Precipitating ordered skyrmion lattices from helical spaghetti and granular powders

Dustin A. Gilbert,[1,2,*] Alexander J. Grutter,[1] Paul M. Neves,[3] Guo-Jiun Shu,[4,5] Gergely Zimanyi,[6] Brian B. Maranville,[1]
Fang-Cheng Chou,[4] Kathryn Krycka,[1] Nicholas P. Butch,[1,3] Sunxiang Huang,[7] and Julie A. Borchers[1]

[1]*NIST Center for Neutron Research, National Institute of Standards and Technology, Gaithersburg, Maryland 20899, USA*
[2]*Department of Materials Science and Engineering, University of Tennessee, Knoxville, Tennessee 37996, USA*
[3]*Center for Nanophysics and Advanced Materials, Department of Physics, University of Maryland, College Park, Maryland 20740, USA*
[4]*Center for Condensed Matter Sciences, National Taiwan University, Taipei 10617, Taiwan*
[5]*Department of Materials and Mineral Resources Engineering, Institute of Mineral Resources Engineering,
National Taipei University of Technology, Taipei 10608, Taiwan*
[6]*Department of Physics, University of California, Davis, Davis, California 95616, USA*
[7]*Department of Physics, University of Miami, Miami, Florida 33146, USA*

Magnetic skyrmions have been the focus of intense research due to their potential applications in ultrahigh-density data and logic technologies, as well as for the unique physics arising from their antisymmetric exchange term and topological protections. In this work we prepare a chiral jammed state in chemically disordered (Fe, Co)Si consisting of a combination of randomly oriented magnetic helices, labyrinth domains, rotationally disordered skyrmion lattices, and/or isolated skyrmions. Using small angle neutron scattering, we demonstrate a symmetry-breaking magnetic field sequence which disentangles the jammed state, resulting in an ordered, oriented skyrmion lattice. The same field sequence was performed on a sample of powdered Cu_2OSeO_3 and again yields an ordered, oriented skyrmion lattice, despite the relatively noninteracting nature of the grains. Micromagnetic simulations confirm the promotion of a preferred skyrmion lattice orientation after field treatment, independent of the initial configuration, suggesting this effect may be universally applicable. Energetics extracted from the simulations suggests that approaching a magnetic hard axis causes the moments to diverge away from the magnetic field, increasing the Dzyaloshinskii-Moriya energy, followed subsequently by a lattice reorientation. The ability to facilitate an emergent ordered magnetic lattice with long-range orientation in a variety of materials despite overwhelming internal disorder enables the study of skyrmions even in imperfect powdered or polycrystalline systems and greatly improves the ability to rapidly screen candidate skyrmion materials.

I. INTRODUCTION

Magnetic skyrmions have emerged as a promising foundation for ultralow-power next-generation memory and logic devices [1–10] and have attracted significant interest for fundamental research due to their exotic antisymmetric exchange interaction and nontrivial topology [11–15]. In natural skyrmion materials, highly ordered monodomain states are prepared by entering the skyrmion stability envelope in temperature and magnetic field, with the field oriented orthogonal to a crystallographic plane with low symmetry in the magnetocrystalline anisotropy [16]. Choosing a low-symmetry orientation nucleates skyrmion domains with a common preferential lattice orientation, promoting a monodomain configuration and demonstrating the critical role of the magnetocrystalline coupling in these materials. The skyrmion lattices can be subsequently reoriented within this plane by introducing a symmetry-breaking anisotropy using an electric field [17], uniaxial pressure [18], or spin-transfer torque [19]. These approaches require that the material have

limited internal disorder and sufficient magnetocrystalline anisotropy to define the orientation of the skyrmion lattice. For materials with weak anisotropy or high internal disorder [7,20–22], the symmetry may be broken in many directions throughout the sample, resulting in a multidomain state. It has been suggested that this multidomain state consists of rotationally disordered skyrmion lattices [23], but it may include other chiral phases depending on the boundary between domains and on the preparation sequence.

The B20-structured intermetallic compound (Fe, Co)Si is unique in that it is a skyrmion material with significant internal disorder even in crystalline form. In this material the Fe and Co atoms randomly occupy the A-site position in the B20 structure, resulting in a random distribution of exchange (defined by the exchange stiffness, A) and Dzyaloshinskii-Moriya interactions [(DMIs) defined by the DMI coefficient, D], and magnetocrystalline anisotropy (K_U). Due to the short-range nature of these interactions (typically approximated by the exchange length, $l \approx 5$ nm) compared to the periodicity of the spin texture (typically >50 nm), the physical characteristics of the chiral skyrmion and helix states are determined by the average of these terms. However, the local variations in A, D, and K_U may act as nucleating and pinning

*dagilbert@utk.edu

defect sites. As typically occurs in polydomain systems, once nucleated, a magnetic domain may propagate until it intersects a pinning defect site or another domain. For misoriented helical states, including the skyrmion state, the intersection of two domains may leave neither able to propagate or reorient, becoming trapped in a jammed state, analogous to magnetic spin ice or frustrated magnets [24,25]. As a result (Fe, Co)Si can possess a complex magnetic state comprising skyrmions, helices [26,27], and/or labyrinth domains (Fig. S1(c) in the Supplemental Material [28]) [29] all of which possess a regular periodicity determined by the average A and D, but not a long-range orientation. Disentangling this complex state requires consideration of the role of topology [9,12], as well as the mechanism for disentanglement, which may involve magnetic monopoles.

In this work, we demonstrate the precipitation of ordered, oriented skyrmion lattices from an otherwise disordered chiral jammed state prepared in a single crystal of (Fe, Co)Si [30]. Rotating the sample in a static magnetic field promotes the formation of hexagonally ordered skyrmion lattices with a common orientation, independent of the initial orientation of the magnetic field relative to the crystal axes. Motivated by the ability to promote ordered skyrmion lattices with an orientation defined by the rotation, a similar approach was applied to a powdered sample of Cu_2OSeO_3. In the powdered sample the weak magnetic coupling between grains yields a state in which each grain nominally consists of a single skyrmion domain that is not aligned with its neighbors. Performing the rotational sequence on the powder also precipitated ordered and oriented skyrmion lattices despite the overwhelming structural disorder. The unexpected promotion of a preferred skyrmion orientation is verified using micromagnetic simulations. Plotting the energy terms from the simulations reveals a close relationship between skyrmion lattice orientation and the magnetic hard axis, although reorientation is promoted even without magnetocrystalline anisotropy. The dissolution of the trapped chiral domains and subsequent formation of ordered skyrmion lattices increases the overall topological charge of the system which may be accompanied by the nucleation of magnetic monopoles.

A 1.5-g single-crystal ingot of $Fe_{0.85}Co_{0.15}Si$ was grown by the Bridgman method in a floating zone furnace, following previously reported methods [31,32]. The [100] and [001] axes of the crystal were identified using x-ray diffraction with Cu $K\alpha$ (1.5418-Å wavelength) radiation. Small angle neutron scattering (SANS) was performed at the NIST Center for Neutron Research on the 30-m NG7SANS beamline [33] using unpolarized 8-Å neutrons and a detector distance of 5 m. The sample was zero-field cooled to 17.5 K; then a saturating field of 500 mT was applied and then reduced to 40 mT for measurement, placing the sample within the skyrmion stability envelope [34]. The magnetic field was applied with an electromagnet along the neutron flight path and initially aligned with the crystalline [100], [110], or [111] axes, as identified in the text; additional data measured with the magnetic field orthogonal to the neutron path are shown in the Supplemental Material [28]. Initial alignment of the sample was achieved by rotating the sample and magnet through $\pm 1°$ (limited by the bore of the magnet). Over this angular range the intensity of the primary helical reflections did not change

substantially, consistent with the large mosaicity values ($>5°$) reported by other authors [23]. Based upon this rocking curve characterization, all measurements were made at an angular position near the rocking curve maximum that preserves right-left symmetry across the detector. We note that the right and left scattering features were determined to individually be maximal at rocking angles of $\pm 0.63°$, which are within the q_z resolution of the SANS instrument when the sample is centered at a rocking angle of zero. All measurements shown here were thus performed at a single rocking angle, as is common practice [34,35–37], since the peak intensities in this configuration do not differ appreciably from the peak maximum.

Except where noted, all SANS measurements were performed with the neutron beam, indicated by n^0, parallel to the magnetic field and orthogonal to the axis of rotation, as shown in Fig. 1(a). During the measurements, the sample was rotated $90°$ stepwise in the static magnetic field about the vertical q_y direction. The rotation direction was then reversed and the crystal returned back to the original orientation, as shown in Fig. 1(a). For example, for the sample initially aligned with $H\|[100]$ the rotation in the (001) plane passed through the [110] crystalline axis, ending at [010] at $90°$; for the sample aligned initially with $H\|[111]$, the rotation in the $(1\bar{1}0)$ plane passed through the [001] and [110] axes. The SANS patterns are identified by ϕ, the sample's cumulative angle of rotation (sequential rotations of $90°$ clockwise, then $90°$ counterclockwise, for example, are $\phi = 180°$). The scattered intensity was plotted as a function of wave vector q (where $q_y\|[001]$ or $[1\bar{1}0]$) or the azimuthal angle in the q_x-q_y scattering plane, θ, measured counterclockwise relative to the $+q_x$ direction [Fig. 1(a)]. Overall, the rocking curve and orthogonal measurements (Supplemental Material [28]) described above revealed that the transverse width (i.e., mosaicity) of the resultant scattering features did not change substantially during rotation (i.e., with increasing ϕ). Rotations at lower temperatures and fields are described in the Supplemental Material [28].

A second sample of powdered Cu_2OSeO_3 was fabricated from CuO and SeO_2 precursors as described previously [38]. The 50-mg sample comprised misoriented crystallites with diameters of >500 nm. The powder was pressed and sintered at 573 K to form a weakly bound pellet and placed in an aluminum foil packet for measurement. SANS measurements were performed using 7-Å neutrons and a detector distance of 15 m after zero-field cooling to 57 K, applying a saturating field of 500 mT, then measuring in a field of 23 mT [39]. Due to the disklike shape of the pressed powder, the sample is always measured in the same orientation relative to the applied field and ϕ is only measured in increments of $180°$, which corresponds to a clockwise rotation $90°$ in the applied field followed by a counterclockwise rotation of $90°$ to return the sample to its original orientation. SANS results are processed by subtracting the scattering pattern measured above the Curie temperature from the measured data to remove structural scattering.

Simulations were performed on the object-oriented micromagnetic framework (OOMMF) platform [40–43] using a 3-nm cubic mesh, with a grain modeled as a cylinder with a 300-nm diameter and 150 nm long and a second simulation of
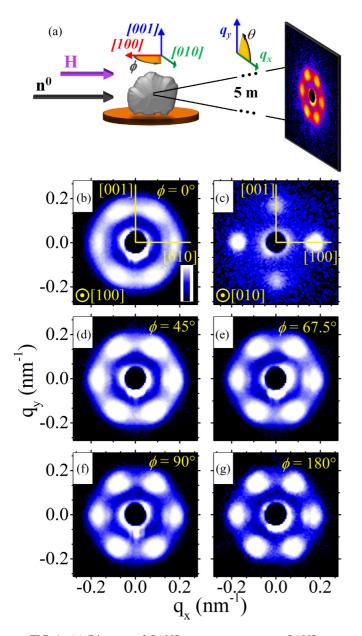
FIG. 1. (a) Diagram of SANS measurement setup. SANS patterns for (Fe, Co)Si initially aligned with the $H\|[100]$ axis measured (b) with $n^0\|[100]$ and (c) $n^0\|[010]$. SANS patterns with $H\|n^0$ rotating the sample in the (001) plane by $\phi =$ (d) 45°, (e) 67.5°, (f) 90°, then (g) back to the initial orientation ($\phi = 180°$).

a rectangular cuboid (parallelepiped) grain 300 nm × 300 nm × 150 nm. The surfaces along the short axis are coupled by periodic boundary conditions, effectively forming a long rod. The magnetic field is applied orthogonal to the short axis such that the skyrmions always have a finite length. For the cylinder the sample geometry makes the geometric contributions the same at every angle of rotation. A cubic magnetocrystalline anisotropy was included with a random site-by-site strength between $K_U = 0$ and 50×10^3 J/m^3, reflecting the random Fe and Co occupancy, with the easy axes oriented along the initial field direction and axis of rotation. We use an exchange stiffness of 1×10^{-11} J/m, saturation magnetization of 1×10^6 A/m, Dzyaloshinskii-Moriya coefficient of

5×10^{-3} J/m^2, and the applied magnetic field was 800 mT. These values were chosen to stabilize the skyrmion spin texture at a size, magnetic field, and simulated temperature approximately matching the experimental system, but were not precisely measured. The orientation of the resultant skyrmion lattice was determined using a fast Fourier transform (FFT). The skyrmion lattice is shown in Fig. 6 from the x ($\phi = 0°$–45°, $\phi = 135°$–180°) or y axis ($\phi = 56°$–124°), to minimize parallax.

II. RESULTS

Magnetometry measurements of the (Fe, Co)Si crystal performed at 10 K show minimal hysteresis or remanent magnetization indicating weak magnetocrystalline anisotropy, consistent with previous results [23]. Consequently, we expect minimal coupling between the magnetic lattice and the crystalline axes.

The skyrmion state was prepared in the (Fe, Co)Si sample by zero-field cooling to 17.5 K, applying a saturating field of 500 mT parallel to the [100] axis, and then reducing the field to 40 mT. At this temperature and magnetic field the (Fe, Co)Si is expected to form skyrmion spin textures, but not skyrmion lattices with long-range order, shown explicitly in Fig. 1(d) of Ref. [34]. Specifically, the magnetic field defines the orientation of the skyrmion tubes while the orientation of the skyrmion lattice, which can be considered to be three helices at 60° rotation, is typically determined by the magnetocrystalline coupling to the crystal lattice. Reducing the magnetic field from saturation, the system initially enters a conical phase, with the propagation along the magnetic field direction. Passing into the skyrmion stability window, the conical phase dissolves, and propagates new helices rotated 90°, now in the plane orthogonal to the field. The orientation of the helices is typically determined by the magnetocrystalline coupling to the underlying crystal lattice. However, due to the weak magnetocrystalline anisotropy in this system, the helices have no orientation. In one scenario, the absence of a dominant propagation direction leads to poor relative alignment of the skyrmion lattices. It has been previously reported that the observed disorder is suggestive of a metastable state consistent with "weakly stratified skyrmion lines" [34,44]. It is possible that the domain nucleation/propagation sequence leads to trapped regions, or domains, bounded by other misaligned domains, which possess chiral structures that are not traditional sixfold skyrmion lattices. In another scenario, the nucleated helices propagate and intersect other domains without establishing the triple helix structure of a skyrmion. The resultant structure may be more stable as a helix, for example, rather than as a skyrmion. Furthermore, the large spatial distribution of the random unit cell occupancy of the Fe and Co atoms leads to large local variations in the exchange and DMI energies, as well as the magnetocrystalline anisotropy. Many of these unit cells—including the parent compounds FeSi and CoSi—do not support a skyrmion phase at all. Accordingly, these sites will likely act as pinning or nucleation sites, and in more extreme cases may possess magnetic ordering that does not reflect a skyrmion spin texture at all. In reality, the physical distinction between these two scenarios may be subtle, and

both magnetic states will give rise to a ring or spherical shell of scattering in reciprocal space.

SANS measurements taken in these conditions show a weak hexagonal pattern sitting atop a uniform ring of scattering, Fig. 1(b). The hexagonal SANS pattern indicates a hexagonally ordered scattering potential in the plane orthogonal to the neutron beam. For this material, the hexagonally ordered pattern has been associated with ordered skyrmion lattices with a common orientation, while the uniform ring is associated with a collection of features with no net orientation, but a regular periodicity, such as labyrinth domains of uniform width (Fig. S1(c) [28]), randomly oriented helices, or rotationally disordered skyrmion lattices (Fig. S1(g) [28]). For reference, labyrinth domains have been previously observed in similar materials, and produce a ring in the Fourier transform [12], as detailed in the Supplemental Material [28]. Disordered helices and skyrmion lattices with a uniform periodicity can also give rise to a ring in the SANS pattern in the absence of a long-range orientation; e.g., the system must be multidomain. Multidomain skyrmions with exactly two orientations have been previously observed and yield a 12-fold SANS pattern. Attempting to fit our data [Fig. 1(b)] to a 12-fold pattern very poorly describes the data and results in a large χ^2 value of 56; we conclude that the multidomain state must consist of more disorder than can be described by a simple two-domain picture, an interpretation which is further supported by the broad azimuthal width of the sixfold peaks.

The sixfold pattern in these measurements is oriented with maxima at $\theta = 0°$, $60°$, and $120°$. Since the SANS pattern is a Fourier transform of the real-space structure, this orientation of the sixfold pattern corresponds to a hexagonal skyrmion lattice with nearest neighbors aligned along $\theta = 30°$, $\theta = 90°$ (the axis of rotation), and $\theta = 150°$. Details of the candidate magnetic structures and their scattering patterns are provided in the Supplemental Material [28]. Using simulations to construct a multidomain state consisting of labyrinth domains and rotationally disordered skyrmion lattices qualitatively reproduces the experimental observations, as demonstrated in Fig. S1 in the Supplemental Material [28].

SANS patterns measured in the orthogonal configuration [e.g., with $H\|[100]$ and neutron beam along [010], Fig. 1(c)] show two diffraction peaks along the horizontal q_x axis (now corresponding to the [100]) and two along the vertical q_y axis (corresponding to the [001]). The two dots along the vertical axis arise from the intersection of the scattering plane with the ring observed in Fig. 1(b), while the horizontal dots indicate a standard helix structure along the [100] direction. These SANS patterns together identify the presence of three magnetic features: (1) an ordered, oriented skyrmion lattice in the (100) plane; (2) a multidomain state comprising some undetermined combination of labyrinth domains, randomly oriented helices, or rotationally disordered skyrmion lattices also in the (100) plane; and (3) a helix propagating along the [100] direction. These orthogonal measurements also demonstrate that the SANS features, and associated disorder, are restricted predominantly to the plane orthogonal to the field direction, as the narrow q_x width of the reflections indicates the skyrmion tubes are well aligned with the field.

Returning to the original measurement configuration described in Fig. 1(a) and shown in Fig. 1(b), the sample was

incrementally rotated in the (001) plane from its original alignment with $H\|[100]$ to $H\|[010]$, shown in Figs. 1(d)–1(f). As the sample is rotated, the sixfold symmetry becomes much stronger, suggesting growth of the skyrmion phase and an enhanced collective orientation of the skyrmion domains. Rotating the sample back to the $H\|[100]$ direction (corresponding to $\phi = 180°$), the sixfold structure gains even more intensity and becomes more pronounced, Fig. 1(g). At $\phi = 180°$ the sample is in its original orientation, but the scattering pattern is clearly different from that of the initially prepared state. The observed changes thus are not an artifact of the sample geometry, but rather originate from an irreversible growth of the skyrmion phase and enhancement of its orientation. Throughout this rotation there is little change observed in measurements taken from the orthogonal perspective [in a configuration analogous to Fig. 1(c), with the neutron beam perpendicular to the magnetic field], shown in Fig. S2 in the Supplemental Material [28].

To better identify the details of the ordering we focus on the emergence of sixfold periodicity by performing an angular-resolved azimuthal projection of the SANS patterns for $0.11\,\mathrm{nm}^{-1} < q < 0.25\,\mathrm{nm}^{-1}$. The azimuthal projection, Figs. 2(a) and 2(b), shows the integrated intensity in the defined q range versus the angle θ in the q_x-q_y scattering plane. In the as-prepared state the projection shows a periodic pattern well offset from the baseline. As the sample is rotated through $0° \leqslant \phi \leqslant 45°$ the amplitude of the periodic features increases while the baseline from the ring remains nearly constant, Fig. 2(a). It is striking that changes in the sixfold structure, which are attributable to the skyrmions, occur without corresponding changes in the ring feature, suggesting that there is no direct conversion between the magnetic phases. This behavior supports the conclusion that the ring is not due to simply rotationally disordered skyrmion lattices. Rotating the sample further, for $45° < \phi \leqslant 90°$ the amplitude of the oscillations remains largely constant while the ring intensity decreases, Fig. 2(b). Rotating the sample back to its original alignment ($\phi = 180°$), the amplitude increases and the baseline decreases.

The azimuthal projection is modeled by six coupled Gaussians from the commonly oriented skyrmions, constrained to be separated by $60°$, and an angle-independent vertical offset from the ring feature: $I(\theta) = C + \sum_{j=0}^{5} A_j\, e^{\frac{[\theta - \mu - (60j)]^2}{2\sigma_j^2}}$, where C corresponds to the underlying ring; A_j and σ_j are the amplitude and width of each Gaussian, respectively; and μ is the average orientation of the skyrmion lattices relative to the q_x axis. This fit converged for each dataset with a reduced χ^2 of <1.2. The average width of the fitted Gaussians, Fig. 2(c), decreases by $>30\%$ during the $180°$ ϕ rotation, indicating improved rotational alignment of the skyrmion domains; the decrease is well fitted by an exponential decay function, $\sigma(\phi) = \sigma_0 + Ae^{\phi/t}$, asymptotically approaching a width of $11°$. Note that the fit for an alternative model with 12 peaks, representing two discrete skyrmion domains oriented along the magnetic easy axes, was extremely poor and converged to a χ^2 of 56.

A simple phase fraction of commonly oriented skyrmions versus misoriented skyrmions, labyrinth domains and randomly oriented helices can be calculated by comparing the
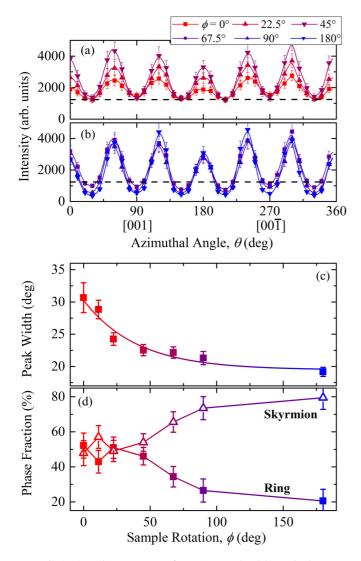
FIG. 2. Annular averages for (a) $\phi = 0°$–$45°$ and (b) $\phi = 67.5°$–$180°$. (c) The azimuthal width of the six peaks of the skyrmion phase and (d) phase fractions from the skyrmion phase and ring phase, determined from their fractional contributions to the scattering intensity.

FIG. 3. (a) Summations of radial sector averages from Figs. 1(b) and 1(d)–1(g), taken at increments of $60°$ with $\Delta\theta = \pm 3.5°$ starting at $0°$ and $30°$, capturing the radial distribution of the ring and skyrmion phases, respectively. Half of the data symbols are not shown for clarity. (b) Peak center and width for the sector averages of the ring and skyrmion features as a function of the sample rotation angle.

integrated weight of the individual contributions to the total scattering pattern, shown in Fig. 2(d). This integration posits that the mosaicity, corresponding to the distribution of the skyrmion tube alignment, remains approximately constant upon rotation, and does not include any ferromagnetic phases or helices oriented along the field direction. As described above, this assumption is supported by both rocking curve and orthogonal measurements (Fig. S2 [28]) of the transverse width [23]. Since the SANS measurement does not capture these magnetic configurations, the simple phase fraction compares the long-range ordered skyrmion phases against the disordered structures responsible for the ring. Interestingly, as the sample is rotated through the first $45°$ the phase fraction of oriented skyrmions changes very little, from 50% to 54%. This change is surprisingly small considering the apparent amplitude change in Fig. 2(a), but arises due to the commensurate decrease in the azimuthal peak width. On the other hand, the phase fraction of oriented skyrmions grows
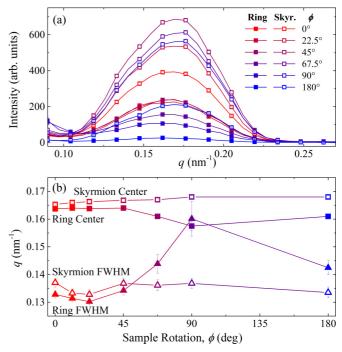
considerably over the subsequent rotation $45° < \phi \leqslant 180°$, reaching a maximum of 80%.

Ordering of the skyrmion features can also be investigated by averaging the intensity versus q over discrete sectors. Two sector averages are presented here, overlapping with the sixfold feature and the interstitial spaces, thus capturing the skyrmion and ring features separately. Each individual sector spans a range of $\pm 3.5°$: $I(q) = \sum_{j=0}^{5} \int_{-3.5}^{3.5} I(q, 60° j + \theta) d\theta$ for the skyrmions and $I(q) = \sum_{j=0}^{5} \int_{-3.5}^{3.5} I(q, 60° j + 30° + \theta) d\theta$ for the ring. The sector averages from Figs. 1(b) and 1(d)–1(g), shown in Fig. 3(a), and their collated trends with sample rotation angle ϕ, Fig. 3(b), show that the ring and skyrmion features are both consistently centered at $0.164 \, \text{nm}^{-1} \pm 0.005 \, \text{nm}^{-1}$, corresponding to a real-space periodicity of 77 nm for the skyrmion lattice and for the helical pitch; for a close-packed skyrmion lattice the lattice periodicity is synonymous with the skyrmion "size." These values are consistent with the previously reported skyrmion spacing for (Fe, Co)Si [34,45]. The width of the skyrmion features along the radial direction is relatively insensitive to rotation in ϕ, indicating that this parameter is dominated by local material properties, as suggested above. Together, the trends highlighted in the azimuthal projections (Fig. 2) and sector averages (Fig. 3) imply that ϕ rotation causes the skyrmion domains to develop a collective orientation, and that new skyrmions are being created while the periodicity throughout the system remains relatively constant. All these observations are consistent with deconstructing a

jammed state of chiral domains. Interestingly, approaching a ϕ of 90° the full width at half maximum (FWHM) of the ring feature measured along the radial direction of the SANS pattern increases, potentially identifying a dispersal of the chiral domain periodicity upon approaching the magnetic easy axis; we note that there is no FWHM variation around the magnetic hard axis [27]. The role of the magnetic easy and hard axes in determining the magnetic structure will be also investigated in the micromagnetic simulations.

For the investigations described above, the field was initially aligned along the high-symmetry [100] axis, which coincides with the magnetic easy axis, and the sample was rotated back and forth through the low-symmetry [110] direction, a local magnetic hard axis. For comparison, measurements were also performed with the magnetic field initially along the [110] direction, shown in Fig. 4. The experimental arrangement is similar to Fig. 1(a), with the [110] aligned with the neutron beam. In this configuration the plane orthogonal to the magnetic field has only one easy axis (namely, the [001] direction), which would typically define the orientation of the skyrmion lattice. However, the SANS measurements [Fig. 4(a)] once more show both the ring and sixfold features, indicating mixed helix/labyrinth phases and rotationally disordered skyrmion lattices. As the sample is rotated by $\phi = 180°$ in the (001) plane, the sixfold lattice is resolved once more [Figs. 4(b)–4(d)], shown in detail in the azimuthal projection [Fig. 4(e)]. Rotating the sample in a static field again promotes a common orientation of the skyrmions [Fig. 4(f)] and breaks up the disordered phase to precipitate the ordered skyrmion phase. Consequently, the skyrmion phase fraction is increased from 37% to 79%, Fig. 4(g). It is also noteworthy that, as in the previous case, the ring feature does not significantly decrease in magnitude during the first 45° rotation (Figs. 1 and 2). This behavior suggests that 45° of net rotation is required to significantly change the magnetic structure, regardless of the magnetocrystalline anisotropy.

Similar rotations were also performed in the (110) plane, starting with the field parallel to the [111] axis; recalling Fig. 1(a), the [110] sample axis is oriented vertically, and the [111] axis is oriented parallel to the neutrons. The [111] axis is the global magnetic hard axis, Fig. 4(h), and as such is a special case for any magnetocrystalline contributions. As the sample was rotated by $\phi = 90°$ [through the [001] axis, Fig. 4(i)] and $\phi = 180°$ [through the [110] axis, to the [$\bar{1}\bar{1}\bar{1}$] magnetic hard axis, Fig. 4(j)], the ring transformed to develop the sixfold pattern. After the rotation, the orientation of the skyrmion lattice is the same as that obtained after rotating in the (001) plane. The skyrmion lattice orientation in this material thus appears to be determined by the rotation direction and not by the magnetocrystalline anisotropy. In other systems such as MnSi, which possess stronger magnetocrystalline anisotropy, the crystalline axes clearly determine the skyrmion lattice orientation, even under rotation [13,46]. This is a strong distinction from the presented work: Rotating skyrmion materials with large magnetocrystalline anisotropy the system undergoes a series of rotations to reflect the changing magnetocrystalline axes, while this work demonstrates a hysteresis associated strictly with the rotation plane. Outside of the skyrmion stability window, rotation of the sample promotes an oriented helix, destroying any precursor state, as shown in Fig. S5 in the Supplemental Material [28].
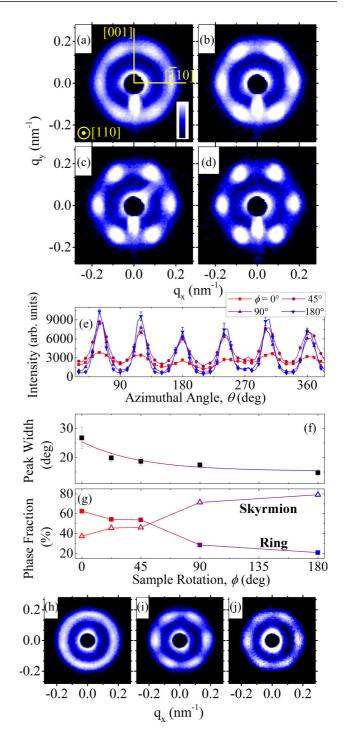

FIG. 4. SANS patterns for (Fe, Co)Si initially aligned with the $H \parallel [110]$ axis measured (a) along the [110] axis, then rotated in the (001) plane by (b) 45°, (c) 90°, then (d) rotated back to 0° ($\phi = 180°$). (e) The azimuthal projection of the data, (f) width of the six peaks of the skyrmion phase, and (g) phase fractions from the skyrmion phase and ring phase, determined from their fractional contributions to the scattering intensity. (h) SANS pattern after saturation along the [111] axis, and rotation by (i) $\phi = 90°$ and (j) $\phi = 180°$.

Rotation-induced promotion of the skyrmion phase along both high- and low-symmetry axes suggests that the skyrmion-ordering mechanism is independent of the initial orientation of the magnetic field relative to the

magnetocrystalline easy/hard axes. We examine this premise in the limit of extreme disorder by performing the skyrmion-ordering sequence on a powdered sample of Cu_2OSeO_3. The nature of this sample—comprising mostly segregated, randomly oriented grains—mandates that skyrmion lattices will form in the plane orthogonal to the magnetic field with random orientations and that the interactions between domains will be comparably small. To clarify, we expect each grain to consist of a single ordered skyrmion lattice, with an orientation defined by the local crystalline orientation and little to no correlation in orientation among neighboring grains; this is not equivalent to the chiral jammed state discussed above. Furthermore, since SANS captures the contributions from the whole sample, the magnetocrystalline anisotropy will not play a net role but will manifest as a highly localized potential landscape promoting or resisting the skyrmion lattice migration during rotation. In the powder sample, symmetry breaking is realized only by the rotation in the plane orthogonal to the vertical direction in Fig. 1(a).

SANS measurements of the as-prepared Cu_2OSeO_3 sample at 57 K after zero-field cooling, then applying a saturating 0.3 T magnetic field, then reducing to a measurement field of 23 mT [Fig. 5(a)] show the ring structure expected for a powder sample, with a radius of $0.103\,nm^{-1}$ (corresponding to a periodicity, and skyrmion size, of 61 nm). Rotating the sample back and forth in increments of $\phi = 90°$, through up to eight cycles [$\phi = 1440°$, Figs. 5(b)–5(d)], causes the emergence and strengthening of a sixfold hexagonal pattern, indicating a net orientation of the skyrmion domains. The sixfold pattern shows maxima along $\theta = 30°$, $90°$, and $150°$, a $30°$ rotation relative to the (Fe, Co)Si single crystal. The Fourier transform of the SANS pattern indicates that the real-space skyrmion lattice orientation has nearest neighbors aligned along the direction orthogonal to the rotation axis, e.g., in the rotation plane, along $\theta = 0°$ and $\pm60°$. An azimuthal projection of the data at $0.07\,nm^{-1} \leqslant q \leqslant 0.13\,nm^{-1}$, Fig. 5(e), shows no significant periodic feature in the as-prepared sample indicating that any helices and/or skyrmion domains are randomly aligned, with their orientation defined locally within each grain. Performing the rotational sequence, Figs. 5(f) and 5(g), the azimuthal projection of the rotated sample has a clear sixfold periodicity; calculating the phase fraction from the feature weight, the ordered skyrmion phase with this orientation accounts for $16 \pm 0.7\%$ of the sample.

III. DISCUSSION

In two different systems we have experimentally demonstrated the ability to precipitate and grow ordered, oriented skyrmion lattices from disordered, coplanar chiral structures, even in the face of overwhelming intrinsic disorder, by rotating the sample in a magnetic field. In the single crystal (Fe, Co)Si the internal chemical disorder and weak magnetocrystalline coupling is expected to nucleate helical phases throughout the sample. These magnetic configurations may locally propagate but become jammed by intersecting other chiral configurations. In our experimental procedure, the sample is saturated; then the magnetic field is reduced to the nominal center of the skyrmion stability envelope. As the field is reduced, the sample will initially relax into a conical phase
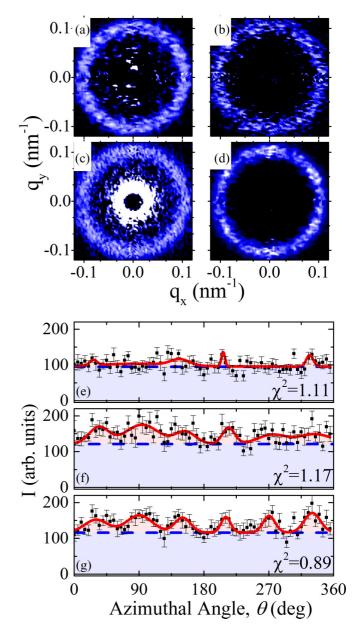

FIG. 5. SANS patterns from powdered Cu_2OSeO_3 taken at (a) $\phi = 0°$, (b) $360°$, (c) $720°$, and (d) $1440°$. Azimuthal projections of the (e) $\phi = 0°$, (f) $720°$, and (g) $1440°$, obtained at $q = 0.11 \pm 0.035\,nm^{-1}$.

oriented along the field direction. Approaching the skyrmion stability envelope, helices nucleate in the plane orthogonal to the magnetic field, presumably from randomly distributed defect sites. These newly nucleated states will consist of three coplanar helices oriented at $60°$, forming a skyrmion state. In the absence of a significant magnetocrystalline anisotropy there will be relatively weak relative orientation between domains of these skyrmion domains. Furthermore, the randomly distributed nucleating sites will mean that the spacing between domains will not be an integer multiple of the skyrmion pitch. Accordingly, the resultant state may possess many misaligned skyrmion domains, as well as other stable helical configurations resulting from the unmatched termination at the boundary of the domains [34,47]. The resultant magnetic

configuration would become jammed, with neighboring regions possessing different magnetic configurations, unable to expand and thus lacking long-range rotational order. Rotating the samples in a magnetic field not only promotes the formation of new skyrmions, and therefore varying the total topological charge of the system, but also overcomes any jamming and causes disordered helical domains to align while conserving their topology.

Recent works have similarly observed the augmentation of skyrmion lattices in single crystals under rotation [13,46]. In these works, it was reported that the SANS pattern for MnSi undergoes a sixfold to 12-fold to sixfold sequential transformation when passing through low- and high-symmetry axes. We report similar results on a MnSi single crystal in the Supplemental Material [28]. This behavior is distinctly different from that observed for (Fe, Co)Si, which shows only a persistent decrease in the second minority phase and indifference to the crystalline axes. The contrast between the response of MnSi (Supplemental Material [28] and Refs. [13,46]) and (Fe, Co)Si to field rotation emphasizes the role of the magnetocrystalline anisotropy in skyrmion formation.

Similarly, the powdered Cu_2OSeO_3 sample shows an enhancement of the sixfold symmetry that emerges with rotation. Previous works, however, have shown that the rotation of a Cu_2OSeO_3 single crystal can cause additional peaks to emerge in the SANS pattern [13], suggesting that the magnetocrystalline anisotropy plays a role in this system, as in MnSi. In the powdered sample, the skyrmion lattices are expected to nucleate within each grain with an orientation reflecting the local crystallographic orientation. However, the skyrmion lattice orientation is expected to be localized due to poor intergranular coupling and the energy cost in propagating lattices between neighboring grains with incommensurate orientations. One way in which the rotation and magnetocrystalline anisotropy may combine to promote a net order is by breaking the symmetry of the cubic structure within each grain, thus lifting the degeneracy of equivalent easy axes via field rotation. The net result for a sum of many grains would be the depopulation of skyrmion lattices coupled to crystalline axes in the plane of rotation and the subsequent growth of those aligned towards the rotation axis. Comparing the results for (Fe, Co)Si, MnSi, and Cu_2OSeO_3 supports recent reports emphasizing the role of anisotropy in skyrmion material [34,48–53].

To provide a better understanding of the experimental results, analogous simulations were performed on a cylindrical grain in a rotating magnetic field using the OOMMF simulation platform. Bloch-type skyrmions were defined in the initial conditions as downward domains, oriented along $-x$, in a matrix oriented in $+x$ with a smoothly varying domain boundary. A cubic anisotropy was used with the magnetic easy axes along the x, y, and z coordinate axes. Hexagonal lattices of skyrmions were generated with the nearest neighbors adjacent along the axis of rotation at $\theta(t = 0) = 30°$, $90°$, and $150°$ [left column in Fig. 6(a)]. Complementing this, hexagonal lattices of skyrmions were generated with the nearest neighbors adjacent in the plane of rotation at $\theta(t = 0) = 0°$, $60°$, and $120°$ [center column in Fig. 6(a)]; the lattices in the left and center columns are related by a $30°$ rotation. The magnetic configuration viewed from the axis of rotation is shown in

the right column of Fig. 6(a), taken from (2). The skyrmion configuration in panel i is the relaxed lattice resulting from the initial conditions. First considering the rotation of the skyrmion tubes (right column), the simulations show that the skyrmion tube direction, which is initially parallel to the easy [100] direction, follows the rotation of the magnetic field, consistent with the SANS results. The skyrmion cross sections appear as ovals rather than stripes due to a deflection of the skyrmion tubes in $-z$ which manifests in the model.

Next, we consider the orientation of the skyrmion lattice during the rotation. The magnetic states at select field angles are shown in Fig. 6(a), panels ii–v, for skyrmion lattices (1) and (2), and the orientation angle of the skyrmion lattices is plotted as a function of sample rotation angle ϕ in Fig. 6(b). These simulation images are from the perspective of the Cartesian axis nearest to the magnetic field, as shown in the illustrative diagrams and in subsequent discussion θ designates the orientation of the skyrmion axis nearest to the horizontal axis perpendicular to the field, e.g., the $+q_x$ direction. In addition to the identified nearest neighbors there are also nearest neighbors at $\pm60°$. At $\phi = 0°$ (panel i) the two skyrmion lattices in the left and center columns are rotated by approximately $30°$ relative to each other, as defined by the initial conditions. The difference in the lattice orientation persists until $\phi = 34°$ (panel ii), at which point lattice (2) undergoes a dramatic shift to $\theta \approx 15°$ to achieve a similar alignment as lattice (1). After rotating the sample to $\phi = 45°$ (panel iii), corresponding to the [110] magnetic axis, both lattices reorient to $\theta \approx 0°$, the initial orientation of lattice (2), with the nearest neighbors in the plane of the rotation (while the [110] direction is not the magnetic hard axis, it is the axis closest to the magnetic hard axis in this plane of rotation). This orientation is directly analogous to that observed for the Cu_2OSeO_3 samples in Fig. 5. Rotating beyond $\phi = 45°$ (panels iv–vi) the lattices retain this approximate orientation (to within $7°$). Enhanced ordering of the skyrmion lattice around $\phi = 45°$ rotation is thus consistent with the experimental results for the (Fe, Co)Si sample in Fig. 2(a), which shows a pronounced reduction in the azimuthal peak width of the skyrmions at this angle, and little change to the skyrmion lattice for $\phi > 45°$. In the simulations a smaller restructuring also occurs at $\phi = 135°$, again passing through the [110] magnetic hard axis, with both lattices retaining a common orientation and returning to approximately $\theta = 0°$ for $\phi \geqslant 135°$. Throughout the rotation there are helical domains which form with periodicity parallel to the magnetic field, particularly on the edges of the simulation volume where the cylindrical curvature is too large to support skyrmions. These helical domains would be invisible in the SANS measurements with the neutrons parallel to the magnetic field, but would appear along the magnetic field direction when viewed (e.g., the neutron path is) orthogonal to the magnetic field. Indeed, Figs. 1(c) and S2 [28], which show the SANS pattern measured orthogonal to the magnetic field, have features located along the magnetic field direction, q_x identifying helical domains.

The simulation results suggest that near the magnetic easy axis the skyrmion lattice prefers a lattice orientation that has the nearest neighbors adjacent in the plane of rotation ($\theta \leqslant \pm5°$), as observed for the powdered Cu_2OSeO_3 sample.
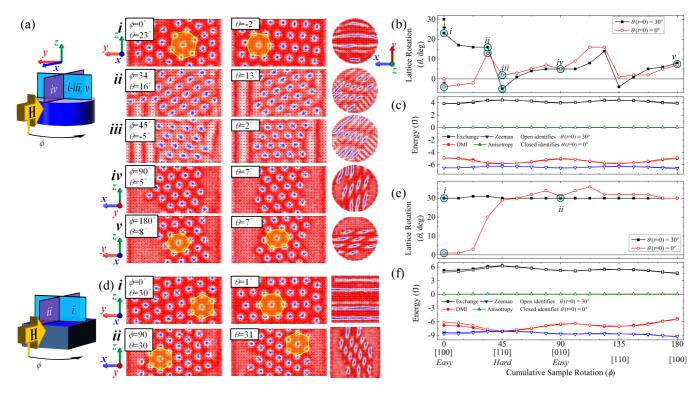
FIG. 6. OOMMF simulation results: (a) magnetic configuration as seen at the bisection of the cylindrical grain, under increasing ϕ ($i-v$), with red indicating the magnetization into the page, and blue indicating out of the page. Left and center columns show the skyrmion lattice with initial orientations ($t = 0$) of $\theta = 30°$ and $0°$, respectively. The lattice is shown from the x axis ($\phi = 0°$–$45°$, $\phi = 135°$–$180°$) or y axis ($\phi = 56°$–$124°$) to minimize parallax, as shown in the illustrative diagrams; images are 306 nm $\times$ 150 nm. Right column shows the magnetization viewed from the direction orthogonal to the plane of rotation; images are 306 nm $\times$ 306 nm. (b) Orientation θ of the skyrmion lattice extracted from the magnetization plots and (c) magnetic energies versus ϕ. Similarly, (d) the magnetic configuration and (e) skyrmion lattice orientation and (f) magnetic energies are plotted versus ϕ for a parallelepiped-shaped grain.

In this orientation the skyrmions push directly against their neighbors during the rotation due to the repulsive skyrmion-skyrmion interaction [54]. Starting along a magnetic easy axis, a dramatic reorientation of the skyrmion lattice occurs as the field direction approaches $45°$, which corresponds to a magnetic hard axis, although the same reorientation occurs even in the case of relatively weak, or even zero, K_U. The energies within the system, shown in Fig. 6(c), correspondingly show inflections at $45°$ for both initial lattice orientations. Along this direction the exchange energy increases while the Zeeman decreases and the DMI grows larger (more negative), indicating an enhanced divergence away from the magnetic field direction, and notably, the anisotropy energy remains constant at approximately zero. Of particular note, there is little difference in the energies for the two models with different initial orientations at $\phi = 0$ (and throughout the entire ϕ range), indicating that the motivating energetics for generating a preferred lattice orientation is dynamic and is not present after the lattice relaxes with the skyrmion tubes aligned with the magnetic field. This behavior is consistent with a driving force of repulsive skyrmion-skyrmion interactions, which would manifest strongly during the dynamic rotation, but would be reduced in the steady-state configuration. Since a reorientation occurs every time the system passes through a magnetic hard axis and the orientation afterwards is the same; rotating the sample repeatedly through hard axes may promote order even in highly jammed systems. Indeed, this

is observed in (Fe, Co)Si which continued to show improved ordering after passing through the [110] direction a second time (between $\phi = 90°$ and $180°$) and in the Cu_2OSeO_3, which required repeated treatments for a total rotation of $\phi = 1440°$ (Fig. 5). Another possible explanation is that forcing the moments to lie along the magnetic hard axis establishes an effective potential energy. After passing the magnetic hard axis, the orientation with nearest neighbors adjacent in the plane of rotation may be the most effective in reducing this energy. Simulations were also performed (not shown) starting along the magnetic hard axis, analogous to Fig. 4, and show a relaxation of the lattice to the same orientation as Fig. 6(a-v). However, for the hard axis simulations, the orientation occurs smoothly and achieves near-full orientation by $\phi = 34°$, approaching the magnetic easy axis. These results, coupled with the skyrmion reorientation at simulated $K_U = 0$, suggest there is an additional contribution potentially attributable to skyrmion-skyrmion interactions.

Simulations were also performed for a rectangular parallelepiped-shaped grain under a rotating magnetic field, Fig. 6(d). This grain will possess additional shape anisotropies absent in the cylindrical grain. As in Fig. 6(a), the system was initially configured with the magnetization parallel to the magnetic easy axis, with $\theta(t = 0) = 0°$ and $30°$ in the left and center column, respectively. Once more the skyrmion tubes follow the rotating magnetic field and undergo a reorientation at $\phi = 45°$. However, for the parallelepiped-shaped grain,

the reoriented lattice has the nearest neighbors aligned along the axis of rotation, Fig. 6(d-*ii*), a 30° rotation relative to Fig. 6(a-*v*). This lattice orientation is directly analogous to the experimental results for the (Fe, Co)Si sample reported in Figs. 1 and 4. The collated lattice orientation, Fig 6(e), confirms both lattices reorient to $\theta = 30°$ and retain this orientation upon further rotation. Once more, the 30° rotation cannot be explained by previous work [46]. The magnetic energies for the parallelepiped-shaped grain, Fig. 6(f), have qualitatively similar features as Fig. 6(c), with inflections around $\phi = 45°$ and again show no significant changes in the anisotropy energies. The difference in the resultant orientation between Figs. 6(a-*v*) and 6(d-*ii*) could be the result of a larger energy barrier at $\phi = 45°$ from the geometry of the simulated grain. However, simulations with large cubic anisotropy ($K_U = 500 \times 10^3$ J/m^3) performed on a cylindrical grain show an orientation following Fig. 6(a), suggesting this is not the case. As another potential source, the cubic simulations show that the skyrmions develop a kink near the grain surface when approaching $\phi = 45°$, presumably to remain orthogonal to the surface. This kink may break the symmetry of the skyrmion lattice and give rise to the preferred orientation with $\theta = 30°$.

Of further interest is the consideration of topology in these systems. Specifically, initial rotations of the (Fe, Co)Si crystal preserve the ring intensity and decrease the azimuthal width of the sixfold feature, essentially promoting a common orientation of the existing skyrmion arrays. This transformation is primarily an in-plane rotation of the skyrmion axis which preserves topological charge. Additional rotations reduce the ring feature and increase the sixfold pattern, consistent with the breakup of labyrinth domains and formation of skyrmions. This process does not preserve topological charge, as the numbers of topological structures before and after the rotation are different. Previous works have identified the mechanism for breaking labyrinth domains into skyrmions via nucleation of zero-moment magnetic monopoles [12]. Monopoles are likely nucleated in the plane of the labyrinth domains and propagate along the magnetic field direction, splitting each domain into two smaller bubble domains. Indeed, these same zero-moment monopoles are observed in our simulations. In addition, the destruction of the skyrmions is realized through the nucleation of a magnetic monopole at the end of the skyrmion tube. In the simulations the skyrmions dynamically annihilate via two mechanisms. In the first mechanism a skyrmion breaks in two along its length, and at the bottom of each tube is a Bloch-point monopole, with equal and opposite charge. The monopole propagates along the skyrmion until it reaches the surface and annihilates. In the second mechanism,

the skyrmion detaches from the surface of the grain, once more nucleating a Bloch-point monopole, which propagates along the skyrmion tube and annihilates at the opposite surface. Thus, beyond the intriguing symmetry breaking and topological charge considerations, the dynamic breakup of the labyrinth domain and annihilation of the skyrmions is accompanied by the nucleation of charged and uncharged magnetic monopoles.

In summary, we demonstrate the ability to precipitate ordered, oriented skyrmion lattices from an otherwise disordered chiral system consisting of rotationally disordered skyrmion lattices, labyrinth domains, and randomly oriented helices by rotating the sample in a static magnetic field [30]. Rotating a single-crystal ingot of (Fe, Co)Si showed a combination of topological charge-conserving lattice reorientation, and skyrmion formation which constitutes a change in the net topological charge of the system. Interestingly, a similar enhancement of the ordering and collective orientation was observed starting along the high-symmetry [100] easy axis or the [110] low-symmetry hard axis. This insensitivity to initial orientation was taken to the limit of complete orientation disorder in a polycrystalline sample of Cu_2OSeO_3. Rotating the powder sample also precipitated ordered, oriented skyrmion lattices. Micromagnetic simulations confirmed the enhanced orientation and promotion of a preferred orientation for different initial orientations with the most pronounced changes occurring when the field is swept through the magnetic hard axis. In all three cases, the dynamic transformation from labyrinth domains to skyrmion lattices constitutes a change in the topological charge of the system by increasing the number of closed topological structures. The ability to precipitate ordered, oriented skyrmion lattices in highly disordered systems enables the study of skyrmion states even in polycrystalline or powdered samples—which are much easier to prepare compared to single crystals—greatly improving the ability to rapidly screen new candidate skyrmion materials.

[1] A. Fert, V. Cros, and J. Sampaio, Nat. Nanotechnol. **8**, 152 (2013).

[2] S. Woo, K. Litzius, B. Krüger, M.-Y. Im, L. Caretta, K. Richter, M. Mann, A. Krone, R. M. Reeve, and M. Weigand, Nat. Mater. **15**, 501 (2016).

[3] D. A. Gilbert, B. B. Maranville, A. L. Balk, B. J. Kirby, P. Fischer, D. T. Pierce, J. Unguris, J. A. Borchers, and K. Liu, Nat. Commun. **6**, 8462 (2015).

[4] L. Sun, R. X. Cao, B. F. Miao, Z. Feng, B. You, D. Wu, W. Zhang, A. Hu, and H. F. Ding, Phys. Rev. Lett. **110**, 167201 (2013).

[5] K. Karube, J. S. White, N. Reynolds, J. L. Gavilano, H. Oike, A. Kikkawa, F. Kagawa, Y. Tokunaga, H. M. Ronnow, Y. Tokura *et al.*, Nat. Mater. **15**, 1237 (2016).

[6] S. A. Montoya, S. Couture, J. J. Chess, J. C. T. Lee, N. Kent, D. Henze, S. K. Sinha, M.-Y. Im, S. D. Kevan, P. Fischer, B. J.

McMorran, V. Lomakin, S. Roy, and E. E. Fullerton, Phys. Rev. B **95**, 024415 (2017).

[7] Y. Tokunaga, X. Z. Yu, J. S. White, H. M. Rønnow, D. Morikawa, Y. Taguchi, and Y. Tokura, Nat. Commun. **6**, 7638 (2015).

[8] P.-J. Hsu, A. Kubetzka, A. Finco, N. Romming, K. von Bergmann, and R. Wiesendanger, Nat. Nanotechnol. **12**, 123 (2017).

[9] W. Jiang, P. Upadhyaya, W. Zhang, G. Yu, M. B. Jungfleisch, F. Y. Fradin, J. E. Pearson, Y. Tserkovnyak, K. L. Wang, and O. Heinonen, Science **349**, 283 (2015).

[10] W. Jiang, G. Chen, K. Liu, J. Zang, S. G. E. te Velthuis, and A. Hoffmann, Phys. Rep. **704**, 1 (2017).

[11] N. Nagaosa and Y. Tokura, Nat. Nanotechnol. **8**, 899 (2013).

[12] P. Milde, D. Köhler, J. Seidel, L. M. Eng, A. Bauer, A. Chacon, J. Kindervater, S. Mühlbauer, C. Pfleiderer, S. Buhrandt *et al.*, Science **340**, 1076 (2013).

[13] L. J. Bannenberg, F. Qian, R. M. Dalgliesh, N. Martin, G. Chaboussant, M. Schmidt, D. L. Schlagel, T. A. Lograsso, H. Wilhelm, and C. Pappas, Phys. Rev. B **96**, 184416 (2017).

[14] A. K. Nayak, V. Kumar, T. Ma, P. Werner, E. Pippel, R. Sahoo, F. Damay, U. K. Rößler, C. Felser, and S. S. P. Parkin, Nature **548**, 561 (2017).

[15] I. Kezsmarki, S. Bordacs, P. Milde, E. Neuber, L. M. Eng, J. S. White, H. M. Ronnow, C. D. Dewhurst, M. Mochizuki, K. Yanai *et al.*, Nat. Mater. **14**, 1116 (2015).

[16] S. Mühlbauer, B. Binz, F. Jonietz, C. Pfleiderer, A. Rosch, A. Neubauer, R. Georgii, and P. Böni, Science **323**, 915 (2009).

[17] J. S. White, I. Levatić, A. A. Omrani, N. Egetenmeyer, K. Prša, I. Živković, J. L. Gavilano, J. Kohlbrecher, M. Bartkowiak, H. Berger *et al.*, J. Phys.: Condens. Matter **24**, 432201 (2012).

[18] A. Chacon, A. Bauer, T. Adams, F. Rucker, G. Brandl, R. Georgii, M. Garst, and C. Pfleiderer, Phys. Rev. Lett. **115**, 267202 (2015).

[19] K. Everschor, M. Garst, B. Binz, F. Jonietz, S. Mühlbauer, C. Pfleiderer, and A. Rosch, Phys. Rev. B **86**, 054432 (2012).

[20] H. C. Wu, T. Y. Wei, K. D. Chandrasekhar, T. Y. Chen, H. Berger, and H. D. Yang, Sci. Rep. **5**, 13579 (2015).

[21] H. Nakajima, A. Kotani, M. Mochizuki, K. Harada, and S. Mori, Appl. Phys. Lett. **111**, 192401 (2017).

[22] T. Matsumoto, Y.-G. So, Y. Kohno, H. Sawada, R. Ishikawa, Y. Ikuhara, and N. Shibata, Sci. Rep. **6**, 35880 (2016).

[23] S. V. Grigoriev, V. A. Dyadkin, D. Menzel, J. Schoenes, Y. O. Chetverikov, A. I. Okorokov, H. Eckerlebe, and S. V. Maleyev, Phys. Rev. B **76**, 224424 (2007).

[24] K. A. Ross, M. M. Bordelon, G. Terho, and J. R. Neilson, Phys. Rev. B **92**, 134419 (2015).

[25] A. M. Samarakoon, M. Takahashi, D. Zhang, J. Yang, N. Katayama, R. Sinclair, H. D. Zhou, S. O. Diallo, G. Ehlers, D. A. Tennant *et al.*, Sci. Rep. **7**, 12053 (2017).

[26] C. Jin, Z.-A. Li, A. Kovács, J. Caron, F. Zheng, F. N. Rybakov, N. S. Kiselev, H. Du, S. Blügel, M. Tian *et al.*, Nat. Commun. **8**, 15569 (2017).

[27] D. Morikawa, X. Yu, K. Karube, Y. Tokunaga, Y. Taguchi, T.-h. Arima, and Y. Tokura, Nano Lett. **17**, 1637 (2017).

[28] See Supplemental Material at http://link.aps.org/supplemental/10.1103/PhysRevMaterials.3.014408 for SANS measurements performed by rotating (Fe, Co)Si in a transverse field, at lower magnetic fields, and outside of the skyrmion stability envelope, and SANS measurements of a MnSi single crystal rotated in an axial magnetic field, and micromagnetic simulations demonstrating the correlation between real-space structure and Fourier transform patterns.

[29] K. Karube, J. S. White, D. Morikawa, C. D. Dewhurst, R. Cubitt, A. Kikkawa, X. Yu, Y. Tokunaga, T.-h. Arima, H. M. Rønnow *et al.*, Sci. Adv. **4**, eaar7043 (2018).

[30] D. A. Gilbert, A. Grutter, P. Neves, G.-J. Shu, F. Chou, K. Krycka, N. Butch, S. Huang, and J. Borchers (unpublished APS March Meeting 2018).

[31] T. Y. Ou-Yang, G. J. Shu, C. D. Hu, and F. C. Chou, J. Appl. Phys. **117**, 123903 (2015).

[32] S. X. Huang, C. Fei, K. Jian, Z. Jiadong, G. J. Shu, F. C. Chou, and C. L. Chien, New J. Phys. **18**, 065010 (2016).

[33] C. J. Glinka, J. G. Barker, B. Hammouda, S. Krueger, J. J. Moyer, and W. J. Orts, J. Appl. Crystallogr. **31**, 430 (1998).

[34] W. Münzer, A. Neubauer, T. Adams, S. Mühlbauer, C. Franz, F. Jonietz, R. Georgii, P. Böni, B. Pedersen, M. Schmidt, A. Rosch, and C. Pfleiderer, Phys. Rev. B **81**, 041203 (2010).

[35] L. J. Bannenberg, R. M. Dalgliesh, T. Wolf, F. Weber, and C. Pappas, Phys. Rev. B **98**, 184431 (2018).

[36] T. Nakajima, Y. Inamura, T. Ito, K. Ohishi, H. Oike, F. Kagawa, A. Kikkawa, Y. Taguchi, K. Kakurai, Y. Tokura, and T.-h. Arima, Phys. Rev. B **98**, 014424 (2018).

[37] S. Seki, J. H. Kim, D. S. Inosov, R. Georgii, B. Keimer, S. Ishiwata, and Y. Tokura, Phys. Rev. B **85**, 220406 (2012).

[38] J.-W. G. Bos, C. V. Colin, and T. T. M. Palstra, Phys. Rev. B **78**, 094416 (2008).

[39] T. Adams, A. Chacon, M. Wagner, A. Bauer, G. Brandl, B. Pedersen, H. Berger, P. Lemmens, and C. Pfleiderer, Phys. Rev. Lett. **108**, 237204 (2012).

[40] S. Rohart and A. Thiaville, Phys. Rev. B **88**, 184422 (2013).

[41] M. Beg, R. A. Pepper, and H. Fangohr, AIP Adv. **7**, 056025 (2017).

[42] V. P. Kravchuk, U. K. Rößler, O. M. Volkov, D. D. Sheka, J. van den Brink, D. Makarov, H. Fuchs, H. Fangohr, and Y. Gaididei, Phys. Rev. B **94**, 144402 (2016).

[43] M. J. Donahue and D. G. Porter, OOMMF User's Guide, Interagency Report No. NISTIR 6376 (U.S. Department of Commerce, Washington, DC, 1999).

[44] U. K. Rößler, A. N. Bogdanov, and C. Pfleiderer, Nature **442**, 797 (2006).

[45] X. Z. Yu, Y. Onose, N. Kanazawa, J. H. Park, J. H. Han, Y. Matsui, N. Nagaosa, and Y. Tokura, Nature **465**, 901 (2010).

[46] Y. Luo, S.-Z. Lin, D. Fobes, Z. Liu, E. Bauer, J. Betts, A. Migliori, J. Thompson, M. Janoschek, and B. Maiorov, Phys. Rev. B **97**, 104423 (2018).

[47] A. Grigorenko, S. Bending, T. Tamegai, S. Ooi, and M. Henini, Nature **414**, 728 (2001).

[48] S. L. Zhang, A. Bauer, D. M. Burn, P. Milde, E. Neuber, L. M. Eng, H. Berger, C. Pfleiderer, G. van der Laan, and T. Hesjedal, Nano Lett. **16**, 3285 (2016).

[49] A. Bauer, A. Chacon, M. Wagner, M. Halder, R. Georgii, A. Rosch, C. Pfleiderer, and M. Garst, Phys. Rev. B **95**, 024429 (2017).

[50] M. N. Wilson, A. B. Butenko, A. N. Bogdanov, and T. L. Monchesky, Phys. Rev. B **89**, 094411 (2014).

[51] F. Büttner, I. Lemesh, and G. S. D. Beach, Sci. Rep. **8**, 4464 (2018).

[52] C. Moreau-Luchaire, C. Moutafis, N. Reyren, J. Sampaio, C. A. F. Vaz, N. Van Horne, K. Bouzehouane, K. Garcia, C. Deranlot, P. Warnicke *et al.*, Nat. Nanotechnol. **11**, 444 (2016).

[53] H. Zhipeng, R. Weijun, D. Bei, X. Guizhou, W. Yue, Y. Bing, Z. Qiang, Z. Ying, L. Enke, X. Feng *et al.*, Adv. Mater. **29**, 1701144 (2017).

[54] S.-Z. Lin, C. Reichhardt, C. D. Batista, and A. Saxena, Phys. Rev. B **87**, 214419 (2013).